



Wall-shear-stress measurements using volumetric μ PTV

Thomas Fuchs¹ · Matthew Bross^{1,2} · Christian J. Kähler¹

Received: 11 November 2022 / Revised: 28 March 2023 / Accepted: 16 May 2023 / Published online: 6 June 2023
© The Author(s) 2023

Abstract

Accurately determining the wall-shear-stress, τ_w , experimentally is challenging due to small spatial scales and large velocity gradients present in the near-wall region of turbulent flows. To avoid these resolution requirements, several indirect iterative fitting methods, most notably the Clauser chart method, exist for determining $\bar{\tau}_w$ by fitting the mean velocity profile further away from the near-wall region in the log-law layer. These methods often require proper selection of fitting constants, assumptions of a canonical flow state, and other empirical-based generalizations. To reduce the amount of ambiguity, determining the near-wall velocity gradient by assuming a linear relationship between the mean streamwise velocity and wall normal distance in the viscous sublayer can be used. However, this requires an accurate unbiased measurement of the near-wall velocity profile in the region below five viscous spatial units, which can be less than 50 μm for high Reynolds number flows. Therefore, in this study a method for a volumetric defocusing microparticle tracking velocimetry method is presented that is capable of resolving the flow in the viscous sublayer of a turbulent boundary layer up to $U_e = 44.7\text{m/s}$ ($Re_\theta = 27250$). This method allows for the measurement of the near-wall flow through a single optical access for illumination and imaging and serves as an excellent complement of larger scale measurements that require near-wall information. The $\bar{\tau}_w$ values determined from the defocusing approach were found to be in good agreement values obtained from a simultaneous parallax PTV measurement. Furthermore, analysis of the diagnostic plot and cumulative distribution of measured fluctuations in the near-wall region, showed that both methods are capable of accurately determining mean velocity and fluctuation profiles in the self-similar viscous sublayer region.

1 Introduction

Accurate knowledge of the mean wall-shear-stress, $\bar{\tau}_w$, for turbulent wall bounded flows is of fundamental interest for many research topics, in particular the aerodynamic or hydrodynamic design and turbulent modeling communities.

The calculation of the skin friction (parasitic) drag of aerodynamic or hydrodynamic bodies also uses $\bar{\tau}_w$. It is estimated that the skin friction drag can contribute to more than 50% of the total aerodynamic drag on subsonic commercial or military airplanes during cruising conditions (Jobe 1984). This estimate is expected to be even higher for large hull ships and submarines (Perlin et al. 2016). Furthermore, the

turbulent skin friction drag can be one order of magnitude higher than the laminar skin friction (Schlichting and Gersten 2016). Therefore, accurate values of $\bar{\tau}_w$ are essential for many industrial/commercial engineering applications.

In principle, determining $\bar{\tau}_w$ for subsonic flows is rather straightforward if the local dynamic viscosity, $\mu = \nu\rho$, of the fluid and the mean velocity gradient evaluated at the wall, i.e., $\bar{\tau}_w = \mu(d\bar{u}/dz)|_{z=0}$, are known. However, accurate near-wall velocity measurements are challenging due to the strong velocity gradients present and spatial resolution requirements, which become even more restrictive with increasing Reynolds number. In the wall bounded turbulence community, $\bar{\tau}_w$ is a fundamental quantity for determining the inner or viscous scaling of the flow. The viscous unit, ν/u_τ , represents the smallest spatial scale in a turbulent wall-bounded flow, where the friction velocity is given by $u_\tau = \sqrt{\bar{\tau}_w/\rho}$. The viscous unit is then in turn used to scale the spatial ($z^+ = zu_\tau/\nu$), velocity ($u^+ = u/u_\tau$), and temporal ($t^+ = tu_\tau^2/\nu$) scales which are important for the development of modeling approaches.

✉ Thomas Fuchs
thomas.fuchs@unibw.de

¹ Institute of Fluid Mechanics and Aerodynamics, Universität der Bundeswehr München, 85577 Neubiberg, Germany

² Fluids Research Department, Applied Research Laboratory (ARL), Pennsylvania State University, State College 16804, PA, USA

As the viscous scales become smaller with increasing Reynolds number, the computational expense for simulations that resolve down to the smallest scales also dramatically increases. Therefore, simulations using coarser grids or reduced order models are used to make these high Reynolds number computations. As the coarser grid simulations do not resolve the smallest scales directly, the small-scale models used by these simulations need to be validated with accurate experimentally obtained information, such as τ_w . Furthermore, in the turbulent regime the fluctuating components and the behavior/scaling of the Reynolds shear stresses are also of interest for the modeling and computational communities. For example, the strength of the near-wall velocity fluctuations and Reynolds stresses is important for determining the location and magnitude of the so-called inner peak. This information is used to develop or validate the universality of Reynolds number-based scaling laws for wall-bounded turbulence (Lee and Moser 2015; Willert et al. 2017; Samie et al. 2018; Smits et al. 2021).

A variety of indirect and direct experimental methods are available for determining τ_w . Detailed and comprehensive reviews of these experimental techniques can be found in Örlü and Vinuesa (2020) and Fernholz et al. (1996). While the focus of this work is not to repeat a review of all available methods, a brief overview of several select techniques is given in the following text.

Floating force elements belongs to the group of direct measurement techniques (Baars et al. 2016). This method directly measures the friction force, requiring a modification of the test facility or model, which is not always possible. Amili and Soria (2011) and Amili et al. (2016) used film-based sensors to estimate the wall-shear-stress from a wall-bounded turbulent flow with a reasonably high temporal bandwidth. Oil film is also commonly used to measure τ_w by relating the interference fringe spacing to the shear force exerted on a thin film of oil applied to the model surface (Schülein 2014; Lunte and Schülein 2020). This method can determine the mean wall-shear-stress very accurately, while it cannot be applied for experiments in water.

Indirect and minimally intrusive surface τ_w measurement techniques include: Surface pressure taps that relate the streamwise pressure gradient with τ_w (Mckee and Smits 2002), surface mounted hot film sensors (Baidya et al. 2019), micro-pillar surface mounted τ_w sensors (Große and Schröder 2008), and temperature sensitive paint (Miozzi et al. 2019). While all of these techniques show merit and success in determining τ_w in the literature, pitfalls of each technique are present. For example, relating average streamwise pressure gradient to τ_w requires that a streamwise pressure gradient exists, which is not the case for the well-studied flat plate boundary layer. Surface mounted hot-film sensor offer the possibility to measure the near-wall turbulence fluctuations up to high-frequencies but the

presence of these films is inherently intrusive, especially when considering the small spatial and temporal scales in the near-wall region.

In order to reduce the complexity of applying the outer-region models, measurements in the viscous sublayer, where the velocity profile is linear with wall normal distance, are highly desired. As previously mentioned, measurements in the near-wall region are challenging due to the strong velocity gradient and small spatial scales. However, using novel optical approaches, high-quality measurements in the near-wall region have been demonstrated in the literature: For instance, single pixel evaluation of PIV recordings (Westerweel et al. 2004; Huisman et al. 2013; Berghout et al. 2021), and by using high magnification PTV (Cierpka et al. 2013; Bross et al. 2019), to list a few.

The experimental determination of flow gradients in the near-wall with sufficient precision is challenging, especially for high Reynolds number turbulent flows where the near-wall viscous scales can be on the order of μm . This coupled with potential facility and instrumentation vibrations during the experiment make the task of accurately measuring the wall-shear-stress non-trivial. Moreover, due the fact that small scales must be resolved in the very near-wall region, it is also necessary to not disturb the flow while conducting the wall-shear-stress measurements in order to avoid biased measurements.

2 Measurement principle

In this optical flow velocimetry approach, the mean wall-shear-stress (WSS), $\bar{\tau}_w$, is estimated from a linear fit of the near-wall velocity profile. To derive the near-wall profile, defocusing microscopic particle tracking velocimetry (defocusing μPTV) is employed (Wu et al. 2005), meaning that a sub-millimeter domain is resolved (Santiago et al. 1998).

2.1 Defocusing PTV

Defocusing PTV is a three-dimensional single camera flow measurement approach, making it suitable for confined and inaccessible measurement domains. The technique relates the geometry of a particle image to the distance of the corresponding particle to the focal plane, i.e., the z location along the optical axis. In x - and y -direction the particle location is defined by the sensor position, X and Y , of the particle image and a scaling function.

Different approaches to determine the particle image geometry can be used: The auto-correlation function, where the particle image boundary is defined by a fixed threshold correlation value (Cierpka et al. 2010b); or the cross-correlation of the particle images with a set of references particle images with well-known locations (Barnkob et al. 2015). In

this defocusing approach, the local intensity distribution at the edges of the particle image are analyzed using an adaptive threshold to determine the edge location with sub-pixel precision (see Fuchs et al. (2016b) for details). Knowing the spatial location of the particles, tracking is used to derive the velocity information from two or more subsequent recordings, yielding a three-dimensional, three component (3D3C) velocity information. To avoid overlapping particle images and generally, due to the large size of the defocused particle images, defocusing PTV requires low particle image densities, such that a nearest neighbor algorithm is sufficient to determine the particle displacements.

2.2 Calibration

Any single camera imaging technique that employs particle image geometries to deduce the spatial particle location requires a function that relates the image information to the physical location. Scanning particles along the optical axis and imaging them at distinct z positions is the most straightforward method to find that relationship for microfluidics (Park and Kihm 2006). However, this scanning procedure is only feasible if there are particles that settle and stay on a surface, which can then be translated along the optical axis. For macroscopic domains, in addition to change of the particle image geometry along z , the scaling in x - and y -direction changes with z , requiring a calibration function depending on all spatial coordinates and not only z (Fuchs et al. 2014).

The particular challenge of this defocusing μ PTV approach for estimating $\bar{\tau}_w$ lies in the fact that it also aims at measuring air flows. Typically, air is seeded with di-ethyl-hexyl-sebacate (DEHS) or water-glycol particles with diameters in the range of 0.3–0.4 μm . It is not feasible to collect samples of these particles on a surface in order to translate them along the optical axis for the purpose of calibration. Moreover, using particles with larger diameters is not a viable workaround, since, at large magnifications, the particle image geometry is strongly influenced by the physical particle size, as shown by Olsen and Adrian (2000).

2.3 In situ calibration

To overcome these drawbacks, the calibration information is derived from the measured data. Such an in situ calibration has demonstrated to be feasible for microscopic as well as for macroscopic defocusing PTV approaches (Cierpka et al. 2010a; Fuchs et al. 2016a; Leister et al. 2021). This calibration procedure is based on the premise that the particle image diameter, D_p , changes linearly with the particle z position along the optical axis, which is a valid assumption at a sufficient distance from the focal plane (Olsen and Adrian 2000).

For the optical configuration used in this study, the assumption of a linear relation between particle image diameter and particle z location yields a maximum deviation of less than 0.4 pixels from the functional relation as introduced by Olsen and Adrian (2000). This deviation is equivalent to a particle z location deviation of around 0.8 μm , considering the slope of the defocusing function. As it is shown in Sect. 4.4, the uncertainty of the particle z location determination lies one order of magnitude higher, which is why the deviation from the linear relation is neglected in the following.

In this defocusing approach, the calibration function that is relating the particle image diameter to the particle z location is derived as follows: The particle image displacements are determined from a set of double-frame images recorded at a certain camera distance, z_c , to the measurement domain. Note that the focal plane is situated such that it lies closer to the camera sensor than the measurement volume. Therefore, with increasing wall-normal particle distance, the particle image diameter, D_p , increases. Toward the wall, i.e., for smaller particle image diameters, the flow velocity and as a consequence also the particle image displacements, ΔX , become smaller and approach zero at the wall. Thus, for a given camera distance, z_c , from the measurement domain, the particle image diameter where the particle image displacement becomes zero can be determined by means of a linear fit of the bin averaged near-wall D_p over ΔX data. This D_p at $\Delta X = 0$ value is denoted by the solid black dot in Fig. 1a for profiles determined at four different camera distances. From the camera distance z_{c_1} to z_{c_4} , the $D_{p,\Delta X=0}$ value increases, since the focal plane is moved further away from the measurement domain.

After conducting the calibration measurements at different well-known camera distances to the measurement volume, the slope, m_d , of the defocusing function can be estimated by means of linear least squares fit, using the $D_{p,\Delta X=0}$ values and the z_c values as input. This step is illustrated in Fig. 1b. Finally, the relation between the particle z location and the particle image diameter D_p can be written as,

$$z = m_d \cdot D_p + t, \quad (1)$$

with t being a z position offset. The x and y scaling, $s_{x,y}$, is determined by a calibration target or by a distinct shape with known geometry that is visible in the camera image, as performed by Leister et al. (2021).

3 Experimental setup and image processing

Estimating $\bar{\tau}_w$, defocusing μ PTV requires only a single optical access, allowing for illuminating and viewing the measurement volume. Microscope optics ensure a high

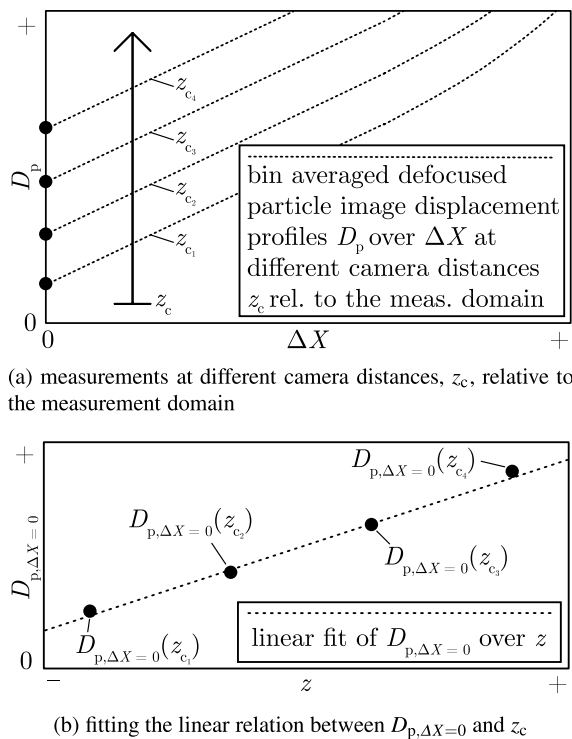
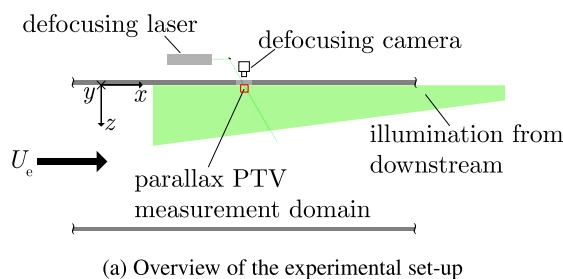


Fig. 1 In situ calibration principle: **a** is illustrating the determination of the diameters where $\Delta X \rightarrow 0$ by a linear fit of the bin-averaged D_p over ΔX data at different camera distances, z_c , relative to the measurement domain. **b** is showing the linear fit of the $D_{p,\Delta X=0}$ over z_c values for estimating the slope, m_d , of the defocusing function

resolution along the optical axis, meaning that the particle image diameter increases strongly with the particle z location relative to the focal plane, which is equivalent to a small m_d value. In particular for large Reynolds numbers, where the viscous scales become small, a high resolution is necessary. The optical components need to be mounted on a translation stage to allow for measurements at different distances from the volume and to compensate for



moving walls. Figure 2 shows a sketch of the experimental setup for determining the wall-shear-stress.

For this study, experiments were conducted in an atmospheric Eiffel type wind tunnel; more specifically in the zero pressure gradient (ZPG) region of a turbulent boundary layer (TBL) model, as detailed in Bross et al. (2019). An overview of the equipment and the experimental parameters is given in Table 1. It turned out to be very challenging to seed the area very close to the wall; there is always a seeding density gradient away from the wall. Thus, a fog generator was used to seed the flow with a water-glycol mixture, upstream of the turbulent boundary layer model. Fog generators have the big advantage that they generate a huge amount of seeding particles, such that the viscous sublayer contains particles. The thickness of the optical access window for the defocusing measurements was 8 mm at a microscope objective working distance of 18.5 mm, such that there was enough space to introduce the volume illumination. Figure 2 gives an overview of the experimental setup.

To derive the particle image geometry, a number of image processing steps were necessary: (1) Each set of recordings was intensity normalized with respect to the first recording of the respective set, to compensate for illumination intensity fluctuations. (2) Employing a stationary contamination on the wall, a (X, Y) sensor vibration correction was performed. This step is required to be then able to (3) calculate an average image of the set, which is then subtracted from each individual image of the set, to remove stationary noise and reflections. (4) The resulting pre-processed images were then used to detect the particle images, exceeding a certain intensity threshold. (5) Finally, the diameters of the detected particle images were determined from the normalized images of processing step (1), combined with a nearest neighbor particle tracking step, using the sensor location (X, Y) and the particle image diameter (D_p) as coordinates.

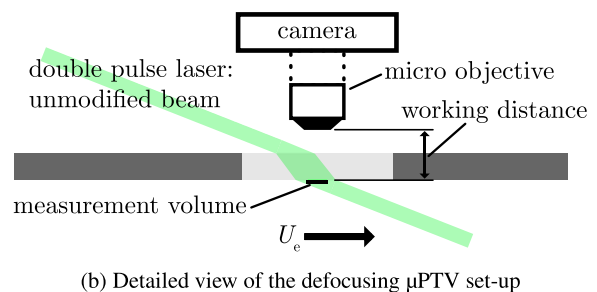


Fig. 2 Experimental setup: The measurements were conducted in the ZPG region of a TBL model in an atmospheric Eiffel type wind tunnel. For the illumination and view of the defocusing μ PTV measurement domain, only a single optical access was needed. To validate the

defocusing approach for the WSS estimation, a parallax PTV reference measurement was performed. This domain was illuminated from downstream and the camera was located on the wind tunnel roof (in negative y -direction)

Table 1 Equipment overview and experimental parameters for the defocusing μ PTV measurements

Camera	LaVision Imager sCMOS
Lens	Zeiss M5X/0.16 420330-9901
Laser	Quantel Evergreen
Microstage	Newport M-UMR8.25
Calibration target	Thorlabs R2L2S3P1
Fog generator	Safex FOG 2010 Plus
Seeding liquid	Safex Inside Normal/Power Mix
Recording software	LaVision DaVis 10
Field of view	$0.97^x \times 1.16^y$ [mm ²]
Scaling in-plane	$s_{x,y} = 0.45$ [$\mu\text{m}/\text{pixel}$]
Magnification	$M = 14.4$ [-]

4 Data processing

4.1 Calibration runs

As outlined in subsection 2.3, an *in situ* calibration approach needs to be performed to estimate the slope, m_d , in Eq. 1, relating the particle image diameter to the z location of the particle. To do so, the near-wall flow was measured at nine different wall distances in steps of $10 \mu\text{m}$ along z , at $U_e = 12.6 \text{ m/s}$ over the TBL model. It has to be noted that it is not strictly necessary to perform these calibration runs at constant conditions, since the only purpose of the procedure is to determine D_p at $\Delta X = 0$. For each run, 3000 double-frames were recorded.

Figure 3 shows the $D_{p,\Delta X=0}$ values at the different wall distances as filled black markers, derived from a linear fit of the near-wall flow; subsection 4.4 provides the details of the fitting procedure. The horizontal error bars in Fig. 3 denote the sensitivity of the manual translation stage, which has a fine adjustment resolution of $10 \mu\text{m}$ (the manufacturer specifies the sensitivity with $1 \mu\text{m}$ for each direction). In vertical direction, the error bars denote the standard deviation of the $D_{p,\Delta X=0}$ values after dividing the sensor into nine equally sized segments, where a linear fit was performed in each segment. The values for the standard deviation do not exceed 2 pixels, indicating that the estimation of $D_{p,\Delta X=0}$ is reasonably robust.

Following the estimation of $D_{p,\Delta X=0}$ at different micro-stage locations, the fit to estimate m_d is performed in the gray area shown in Fig. 3, where the change of D_p along z can be considered linear. At smaller particle image diameters, closer to the focal plane, this approximation does not hold, which can also be seen by the deviation of the $D_{p,\Delta X=0}$ values at $z_s = -40 \mu\text{m}$ and $z_s = -30 \mu\text{m}$ in Fig. 3. For the optical equipment used in this experiment, the slope of the defocusing function yields $m_d = 2.06 \mu\text{m}/\text{pixel}$; that means that the particle z location changes by $2.06 \mu\text{m}$ at a particle image diameter change of 1 pixel.

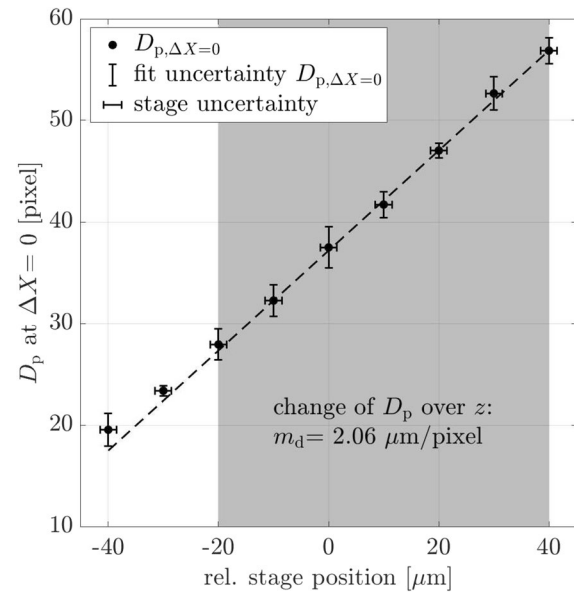


Fig. 3 Calibration function, relating the particle image diameter D_p to the particle z location. The relation is derived from measurements at different camera distances from the measurement domain. At each distance, $D_{p,\Delta X=0}$ is estimated and then fitted with a linear function, leading to a value of $m_d = 2.06 \mu\text{m}/\text{pixel}$ for this optical configuration

4.2 Technical limitations

For the present optical configuration, starting at a minimal particle image diameter of around 30 pixels – at smaller diameters the linear approximation of the relation between D_p and z does not apply anymore – at the wall ($z = 0 \mu\text{m}$), the particle image diameter at a wall distance of $z = 500 \mu\text{m}$ would yield 240 pixels; this is equivalent to 10 % of the sensor X size of 2560 pixel. However, at larger particle image diameters, the SNR of the particle image decreases, such that the number of detected particle locations decreases along the optical axis. As a consequence, using the water-glycol seeding particles with a mean diameter of around $0.3\text{--}0.4 \mu\text{m}$, the particle locations can only be detected up to particle image diameters of around 100–150 pixels, hence around $\Delta z \approx 200\text{--}300 \mu\text{m}$.

It is obvious that at such large particle image diameters, the particle image density and therefore the measurement efficiency is rather low. Overlapping particles images are difficult to employ for the particle location determination, since uncertainty of the location determination becomes larger. Thus, they are rejected entirely to yield a higher accuracy of the estimated velocity field. In addition, it was found difficult to seed the near-wall flow, i.e., the measurement domain of this defocusing μ PTV approach ($z < 200 \mu\text{m}$).

Using a commercially available DEHS seeding generator with 45 Leskin nozzles was not able to provide enough for

the measurements, except for the $U_e = 12.7$ m/s case. Only a fog generator was capable for supplying enough seeding, such that the near-wall measurement were feasible; even then with a very limited seeding concentration. As a consequence, the velocity information captured in each recording decreased from around 2 tracks per image at $U_e = 12.7$ m/s to around 1 track per image at $U_e = 44.7$ m/s. Expressed as a seeding concentration, considering a measurement domain size of roughly $1 \times 1 \times 0.2$ mm³, the concentration lies in the range of 5 – 10 particles/mm³ close to the wall ($z < 200$ μm).

In fact, the seeding is the biggest drawback of using particle imaging techniques for near-wall flow measurements. Apart from the difficulty to supply seeding particles close to the wall, the increasing seeding concentration with the wall-normal distance is problematic, in particular, if it is the goal to measure through a single optical access. For single optical access approaches, imaging systems with a large depth of focus are problematic for the $\bar{\tau}_w$ measurements, since the particle image density limit would require a limitation of the seeding concentration, such that there is relatively little velocity information close to the wall. Microscope objectives, as used for this approach, have a rather small focal depth, such that particles in the background of the view, appear as image noise and not as intensity peaks on the sensor.

4.3 Vibration correction

Processing the recordings included a (X, Y) sensor vibration correction, where a bright intensity peak induced by a contamination sitting on the optical access window served as a reference. For each set of recordings, the camera vibration was determined relative to the first recording of the set. The shift was determined with integer precision using a normalized cross-correlation with a window size of $128 \times 128 \text{ pixel}^2$. These shift values, translated from pixel into physical coordinates using the in-plane scaling $s_{x,y}$ are plotted against U_e in Fig. 4 (black crossmarkers), showing a moderate increase from around 4 μm to about 8 μm with the free stream velocity. However, this (X, Y) correction procedure does not account for the vibration in z -direction, which is equivalent to a correction of the particle image diameter.

Such a correction of the z vibration can be performed by employing a particle that is attached to the wall; note that there was always one or more particles attached to the wall once the seeder was switched on, even after a cleaning procedure. However, it has to be emphasized that this reference particle image is not an image of a particle within the flow. Thus, the characteristics, such as the physical diameter, of this reference particle does not necessarily represent those of the actual seeding particles. Nonetheless, the intensity of the selected reference particle image

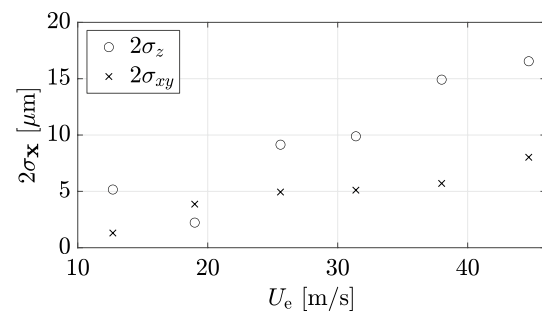


Fig. 4 The standard deviation of the relative movement between the camera sensor and the measurement domain as a function of U_e . With U_e , the motion in xy -direction increases less than z -direction

is not significantly larger than those of the particle images of the moving particles in the flow, which gives rise to the assumption that their diameter lies in the same range. Moreover, the slope of the defocusing function m_d changes by less than 1 % when comparing particles with a difference of one order of magnitude in physical diameter in this size range (Olsen and Adrian (2000)). When conducting the z vibration correction, it also needs to be taken into account that the physical particle diameter could change due to evaporation, considering that a water-glycol mixture was used for seeding the flow. Calculating a moving mean over 100 recordings of the reference particle image diameter over the time of the recording, revealed that the particle image diameter decreased by 1.5 pixels in a linear fashion for the $U_e = 31.4$ m/s data set, for instance. As a consequence, such diameter changes were compensated for in all recorded data sets.

As illustrated in Fig. 4, the z vibration correction becomes more important with an increase of U_e . Thus, $2\sigma_z$ starts at around 2.5 μm at the low U_e sets and reaches up to $2\sigma_z \approx 17$ μm at $U_e = 44.7$ m/s. Here, it is important to emphasize that the characteristics of the movements of the camera relative to the measurement domain were unknown, i.e., it is not clear what is actually moving. Most likely, the movements in x -, y -, and z -direction of part of the setup also differed due to the variable rigidity of the camera mount and the tunnel walls with respect to the spatial direction. In particular, the tunnel wall should be less rigid in wall-normal direction, an assumption that is supported by the stronger increase of the $2\sigma_z$ values in comparison with the $2\sigma_{xy}$ values.

Considering the wall unit size of $z^+ \approx 12\mu\text{m}$ at $U_e = 44.7$ m/s, $2\sigma_z \approx 17$ μm comprises roughly 1.5 wall units, i.e., 30% of the viscous sublayer height, emphasizing the necessity of the z vibration correction. However, for the $U_e = 12.7$ m/s set, the vibration drops to $2\sigma_z \approx 3$ μm, equaling roughly 0.1 wall units, making a correction somewhat unnecessary.

4.4 Wall-shear-stress calculation

The mean wall-shear-stress, $\bar{\tau}_w$, is estimated by a least squares fit of the binned near-wall velocity profile, which is assumed to be linear in the viscous sublayer region. To do so, the measurement data are binned along U and not along the wall-normal coordinate, z , as a result of particle location determination uncertainty considerations.

Generally, employing the particle image geometry for deducing the spatial particle location, the z coordinate, along the optical axis, is less accurate. This is due to the fact that the geometry feature, in this case the particle image diameter, is determined with an uncertainty. Hence, the uncertainty of the diameter determination in combination with the slope of the defocusing function denotes the uncertainty of the particle z location. For this defocusing approach, the particle image center is defined as the location midway between the left and the right vertex of the circular particle image in sensor X -direction, and in sensor Y -direction, midway between the upper and the lower vertex of the circle. Essentially, this is the same procedure as for the determination of the particle image diameter, which is defined as the average distance between the vertices in the respective direction $D_p = (D_x + D_y)/2$. Thus, expressed in pixel values, the uncertainty of the particle image diameter determination and the particle image center location determination is comparable. However, comparing the uncertainty in physical coordinates for this experiment, the uncertainty for the z location is around 4.5 times larger relative to the x and y location. This particular difference is the ratio between the slope of the defocusing function ($m_d = 2.06 \mu\text{m}/\text{pixel}$) and the scaling factor in the in-plane direction ($s_{x,y} = 0.45 \mu\text{m}/\text{pixel}$).

In addition, following consideration leads to the conclusion to use a U binning instead of a z binning: Close to the wall, say at $z < 10 \mu\text{m}$, the flow velocities in wall-normal direction, W , as well as in spanwise direction V should be very small, close to zero. However, due to the uncertainty in the particle location determination, the velocity measurement is not exact, such that the standard deviation of V and W close to the wall provides a suitable measure of the uncertainty of the particle location determination. For the $U_e = 25.6 \text{ m/s}$ case, $2\sigma_V$ is 0.13 m/s , whereas $2\sigma_W$ yields 0.96 m/s , which, translated into a particle location uncertainty, equals $2\sigma_z = 14.3 \mu\text{m}$. With $5z^+ \approx 97 \mu\text{m}$, marking the wall-normal range of the viscous sublayer with its linear velocity profile, $2\sigma_z$ comprises around 15% relative to the sublayer height. In contrast, the uncertainty of a single U measurement value, which is equivalent to the uncertainty $2\sigma_V$, comprises only around 3% of the mean velocity at the edge of the viscous sublayer.

An overview of the U over z measurement values (small grey dots) along with the bin averaged data (black dots for U binned data and red dots for z binned data) for the $U_e =$

25.6 m/s case is given in Fig. 5. The z binned data values differ from those of the U binned points, as such that they deviate from the linear behavior close to the wall location at $z = 0 \mu\text{m}$. Due to the z binning, the slope of the velocity profile is slightly biased toward underestimating the wall-shear-stress, which becomes more evident at larger U_e values. Thus, at $U_e = 12.7 \text{ m/s}$ $\bar{\tau}_w$ is only around -9% lower than compared to the U binning, whereas this underestimation is steadily increasing to up to around -22% at $U_e = 44.7 \text{ m/s}$. This biased $\bar{\tau}_w$ estimation is a result of the uncertainty of the particle z location determination, which increases relative to the decreasing thickness of the viscous sublayer at larger U_e values.

Looking closer at Fig. 5, it becomes apparent that, starting at around $z = 80 \mu\text{m}$, the binned data points do not follow a linear trend to the border of the viscous sublayer edge at $z = 80 \mu\text{m}$ anymore. This is an issue that can be attributed to the defocusing PTV measurement technique: The particle image diameter grows with z , while at the same time the signal to noise ratio (SNR) reduces, making a detection of the particle images increasingly difficult. Additionally, particle image overlaps become more likely at larger particle image sizes. As a consequence, the number of detected particle images decreases with z , even though the seeding concentration increases with the wall distance, resulting in a lack of measured data points. Moreover, at $z > 80 \mu\text{m}$ different behaviors of the bin averaged data points, depending on the binning parameter, can be observed in Fig. 5. The U binned data show an increasing velocity gradient with wall

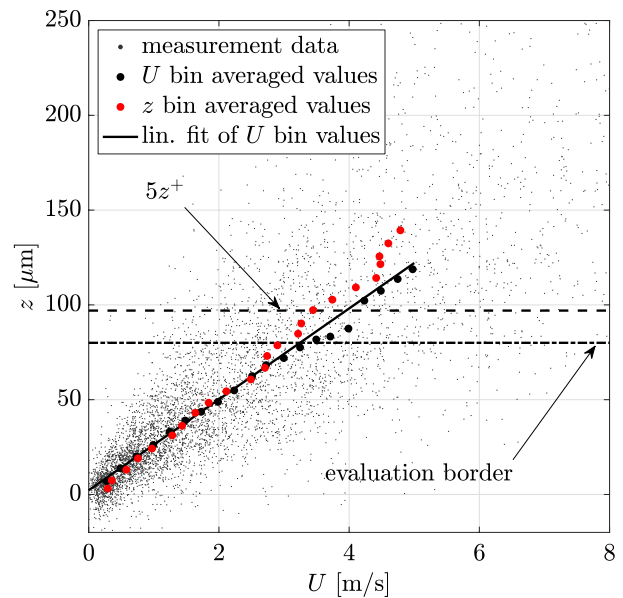


Fig. 5 The measured velocity values U over z . For the linear fit, to derive the wall-shear-stress, U bin averaged values were chosen, since the particle z location uncertainty resulted in a systematic underestimation of $\bar{\tau}_w$ in the case of a z binning

distance, which is the opposite of what happens in a turbulent boundary layer flow. However, this behavior becomes explainable when considering that the number of detected particles decreases with distance to the wall: At $z > 80\mu\text{m}$, using U bins means that the particles at smaller wall distances are overrepresented in the bin, leading to an underestimation of the z location of this U bin, which is equivalent to an overestimation of the velocity at this z location. It has to be emphasized that the deviation of the bin averaged data points starts at around $z > 80\mu\text{m}$. For the $U_e = 25.6$ m/s data set, the U bin located at around $z = 80\mu\text{m}$ comprises measurement points reaching out to around $z \approx 200\mu\text{m}$, giving rise to the assumption that the systematic error due to the problem of not detecting large particle images becomes relevant at $z > 200\mu\text{m}$ for this experimental configuration. Consequently, areas where the particle locations are larger than this z threshold should not be considered for evaluation using this specific optical setup, as indicated by the dot-dashed line in Fig. 5. Unlike the U binned data, the z binned data are not affected by this systematic overestimation of the velocity.

It is obvious that there is a significant number of influencing factors in the defocusing μPTV procedure for deriving the wall-shear-stress. Even more so, it is of utmost importance to analyze the defocusing μPTV technique thoroughly in terms of its validity. To do so, in the following results section, the defocusing μPTV measurement results are compared to those of a parallax PTV approach, serving as a reference. Moreover, a detailed analysis of the near-wall flow provides a more insights on the uncertainty and also the validity of the defocusing μPTV technique, as well as of the parallax PTV reference measurement.

5 Results

5.1 Parallax PTV reference measurements

To demonstrate the feasibility to determine the mean wall-shear-stress from defocusing μPTV measurements, a parallax PTV validation measurement was conducted. Parallax PTV makes use of mirrored particles on a reflective surface, such as a glass window or polished metal, to refine the wall normal location of the particle in terms of a parallax correction (details can be found in Cierpka et al. (2013) and Fuchs et al. (2018)). This reference measurement system imaged the flow in a light sheet in the xz -plane as shown in Fig. 2, while the camera was placed outside of the tunnel, above the upper wall located in negative y -direction as seen from the measurement domain (an overview of the parallax PTV experimental characteristics is given in Table 2). In the following, the results of the parallax PTV measurements serve as a reference for the defocusing μPTV results. The parallax

Table 2 Equipment overview and experimental parameters for the parallax PTV reference setup

Camera	<i>LaVision Imager sCMOS</i>
Lens	<i>Zeiss 2/100 mm Makro Planar</i>
Teleconverters	<i>4 Kenko 2×</i>
Laser	<i>Innolas Spotlight 1000 PIV – 15</i>
Working distance	1.3 m to the sensor
Field of view	$4.4^\circ \times 3.5^\circ$ [mm^2]
Scaling in-plane	$s_{x,z} = 4.0$ [$\mu\text{m}/\text{pixel}$]
Magnification	$M = 1.6$ [-]

recordings were always taken directly after each defocusing run, such that the conditions were similar. As it is done for the defocusing data, $\bar{\tau}_w$ is estimated from a linear fit of the near-wall velocity profile, while the parallax PTV data are binned along the wall-normal z coordinate.

5.2 Wall-shear-stress and near-wall flow: defocusing μPTV vs. parallax PTV

In the present and following sections, the recorded data sets are referred to in terms of their momentum thickness Reynolds number $Re_\theta = U_e \theta / \nu$, as listed in Tab. 3, column 2. The momentum thickness, θ , used for calculating $Re_\theta = U_e \theta / \nu$ was derived from a particle image velocimetry (PIV) measurement, conducted directly after the defocusing and the parallax PTV runs at a specific Re_θ , to ensure similar conditions. The PIV measurement covered a field of view of $270^\circ \times 300^\circ \text{mm}^2$.

It should be noted that the outer region parameters (θ , δ_{99} , etc.) measured and calculated from these PIV measurements are subjected to upstream historical and environmental effects in the atmospheric wind tunnel where these measurements were taken. These upstream historical effects have been shown to influence the shape/topology of the wake region of this boundary layer but, it was shown that the turbulent behavior in the near-wall and log-law layer remains largely unaffected (Knopp et al. 2022). Furthermore, as the focus of this investigation is on the evaluation of a measurement technique capable of accurately estimating the velocity gradient in the very near-wall region, potential non-canonical features in the wake/edge region of the boundary layer do not affect the analysis presented herein.

For this study, $\bar{\tau}_w$ was determined at six different Re_θ values, ranging from 8040 to 27250. The estimated $\bar{\tau}_w$ values show a good agreement between the defocusing and the parallax measurements, comparing columns 4 and 5 in Table 3. However, at $Re_\theta = 27250$, defocusing yields a 6% smaller $\bar{\tau}_w$ value. Further, Fig. 6 illustrates the $c_f = 2U_\tau^2 / U_e^2$ over Re_θ relation compared to an empirical derived theoretical incompressible correlation, as defined by Smits et al. (1983).

Table 3 Overview of the different data sets and their most important parameter and measurement values

U_e [m/s]	Re_θ [-]	θ [m]	$\bar{\tau}_w$ defocusing	$\bar{\tau}_w$ parallax	U_τ [m/s]	$z(z^+ = 5)$ [μm]	δ_{99} [m]	Re_τ [-]
12.7	8040	0.0102	0.23	0.23	0.46	177	0.116	3260
19.0	14,070	0.0120	0.43	0.45	0.62	132	0.127	4830
25.6	18,690	0.0119	0.78	0.76	0.84	97	0.129	6640
31.4	20,260	0.0105	1.14	1.11	1.01	81	0.114	7080
38.0	23,730	0.0102	1.53	1.59	1.17	70	0.110	7880
44.7	27,250	0.0100	2.09	2.27	1.37	60	0.107	8940

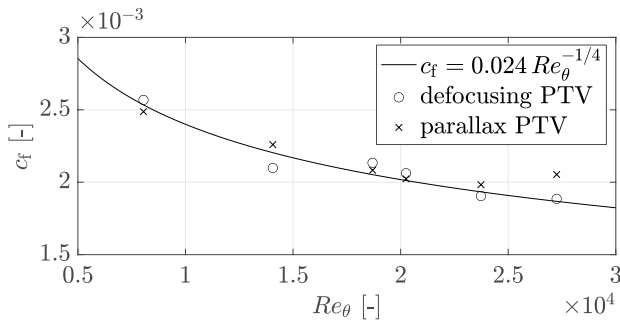


Fig. 6 The skin friction c_f over Re_θ for the defocusing and the parallax PTV measurements, compared with a semi-empirical-based correlation curve as defined by Smits et al. (1983)

Evidently there is a good agreement with theory, with deviations from this correlation of $\sigma_{\Delta c_f, \text{def}} = 3.1\%$ for the defocusing and $\sigma_{\Delta c_f, \text{par}} = 3.9\%$ for the parallax PTV approach.

Apart from the wall-shear-stress, the PTV approaches deliver information of the near-wall velocities and fluctuations. The measurements presented here were conducted in a zero pressure gradient (ZPG) turbulent boundary layer flow, such that they can be represented by inner units, employing the estimated wall-shear-stress for normalization, where friction velocity is calculated from: $U_\tau = \sqrt{\bar{\tau}_w/\rho}$. The U_τ values

for the different Re_θ are listed in column 6 of Tab. 3 and the physical distance of $5z^+$ in column 7.

The mean flow profile $U^+ = U/U_\tau$ over $z^+ = zU_\tau/\nu$ is shown in Fig. 7 for the defocusing and the parallax PTV measurements at three Re_θ values. In this figure, the circles denote the defocusing data, only reaching out to an equivalent of around $80 \mu\text{m}$ from the wall. The parallax PTV data set is divided into two parts: The crossmarkers represent the parallax corrected data points, which reach out to about $700 \mu\text{m}$ from the wall. While using the same recordings for evaluation, data points at larger wall distances were not considered for parallax correction (solid dots), since the quality of the particle mirror images became worse with particle wall distance. Moreover, due to the decreasing velocity gradient with the increasing wall-normal location, the uncertainty of the particle location has less impact, such that a parallax correction becomes less crucial.

At $Re_\theta = 8040$ and $Re_\theta = 14070$, defocusing as well as parallax PTV show a good agreement with the linear region in the viscous sublayer and with the logarithmic layer. A slight underestimation of U^+ can be observed at $Re_\theta = 27250$, indicating an increased measurement uncertainty and an increasing spatial resolution deficit.

The velocity fluctuations for $Re_\theta = 14070$ are plotted in Fig. 8. Again the defocusing values are denoted by circles,

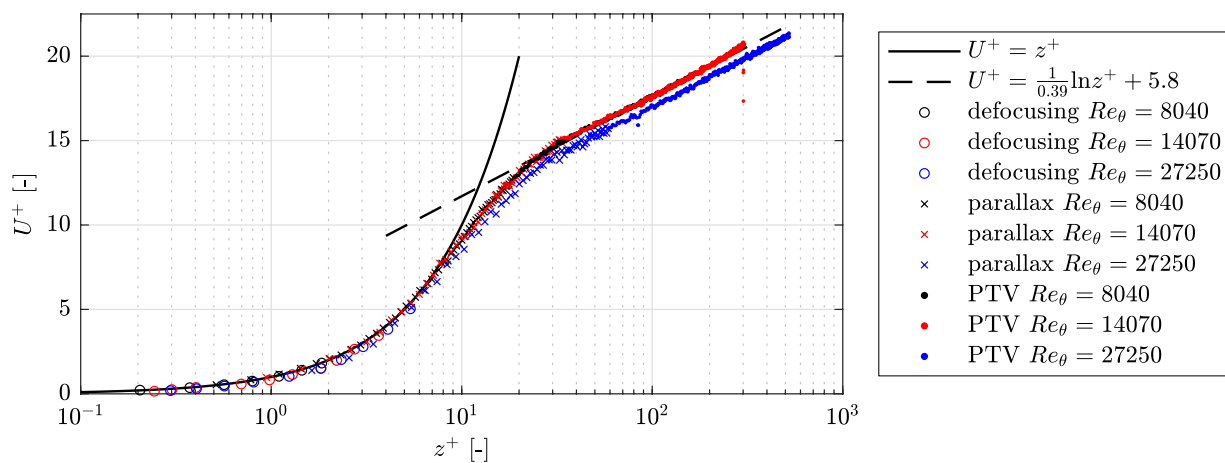


Fig. 7 Mean near-wall velocity profile in inner units at $Re_\theta = 8040$, $Re_\theta = 14070$, and $Re_\theta = 27250$

complemented by plus markers denoting points associated with the spanwise y -component, which can only be provided by the volumetric defocusing PTV technique. The crossmarkers denote the parallax corrected PTV data, whereas the solid dots represents the non-corrected data points at larger wall distances. Here again, defocusing μ PTV and parallax PTV show a fairly good agreement, while the defocusing \bar{u}^2/U_τ^2 values at $z^+ > 10^0$ yield slightly lower values as compared with the parallax data. Approaching the wall, the defocusing \bar{u}^2/U_τ^2 values also increase again, indicating an increasing influence of the wall-normal particle location determination uncertainty. In the following section, the measurement data for both the defocusing and the parallax approach is analyzed in

more detail, to check their validity and also to understand the increasing uncertainties that appear at $Re_\theta = 27250$.

5.3 Validation with diagnostic tools

The so-called diagnostic plot, as proposed by Alfredsson and Örlö (2010) can be employed to validate near-wall flow data in wall-bounded turbulence. For these measurement results, Fig. 9 represents this diagnostic plot, where a self-similarity, i.e., a Reynolds number independence, in the near-wall region ($z^+ < 10$) can be observed. The measured values lie above the theoretical curve, as a result of the particle location determination uncertainty and the particle displacement determination uncertainty, elevating the U_{rms}/U_e value. This bias increases closer to the wall, where the uncertainty of

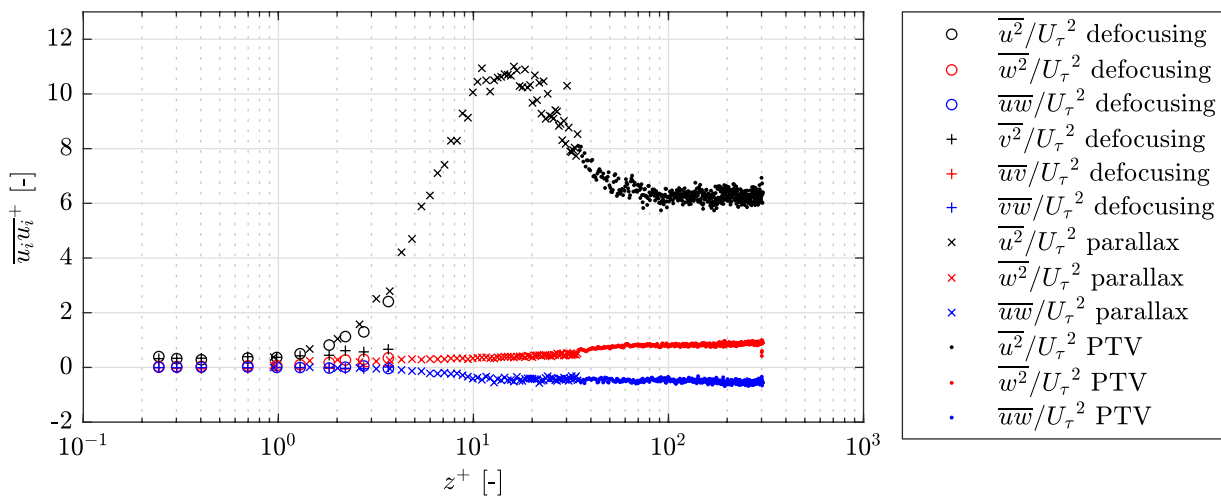


Fig. 8 Near-wall velocity fluctuations in inner unit at $Re_\theta = 14070$. The spanwise y -component is only captured by the volumetric defocusing μ PTV approach

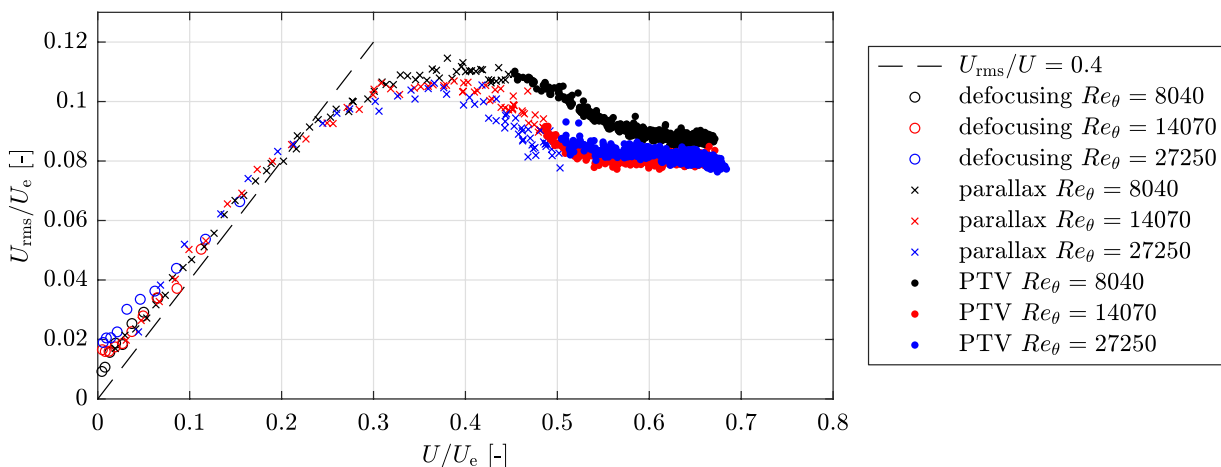


Fig. 9 Diagnostic plot as proposed by Alfredsson and Örlö (2010): Close to the wall, the defocusing μ PTV and the parallax PTV reference results show the expected self-similarity

the particle image displacement determination becomes more dominant, since the absolute particle image displacements become smaller. Thus, at the wall the relative uncertainty of the particle image displacement determination is the largest, as indicated by the systematic deviation from the theoretical line. Moreover, it becomes evident that the bias also increases with Re_θ , since these data points show a larger deviation from the theoretical curve. In general, due to the larger uncertainty of the wall-normal particle location determination, the defocusing PTV approach yields larger U_{rms}/U_e values as compared to the parallax PTV approach. Further away from the wall, the maximum of U_{rms}/U_e decreases with higher Re_θ , as does the location U/U_e of the maxima, both lying in accordance with literature. In terms of the validity of the proposed defocusing PTV approach and also of the parallax PTV reference measurement, this diagnostic plot analysis clearly gives rise to the validity of these near-wall flow measurements.

Further validation assessments involve the cumulative distribution function (cdf), to analyze the velocity fluctuations in the near-wall region. Alfredsson et al. (2011) showed that in the viscous sublayer the fluctuations can be approximated by a log-normal distribution; the distribution is self-similar, and as such, independent of the Reynolds number and the wall distance within the viscous sublayer

($z^+ < 5$). A selection of empirical cdfs, computed using the Kaplan–Meier estimate (Kaplan and Meier (1958)), of the defocusing μ PTV and the parallax PTV data, are plotted in Fig. 10; the distributions are compared to the cdf of a direct numerical simulation, performed at $Re_\theta = 4000$ by Schlatter and Ölö (2010). The fitted parameters of the log-normal distribution were $\mu = -0.069$ and $\sigma = 0.425$. At $z^+ \approx 3$, slightly above the center of height of the viscous sublayer, both defocusing and parallax PTV show a good agreement of the U^+/z^+ distribution in comparison with the DNS reference, as shown in Fig. 10a. As plotted in Fig. 10b, cdfs at different z^+ locations for $Re_\theta = 14070$ show some deviation from the self-similarity. For instance, the black dashed line, representing the parallax PTV results at $z^+ = 0.95$, shows a significant bias at larger as well as at smaller U^+/z^+ values; several effects lead to this bias of the parallax data very close to the wall. One is that the relative uncertainty of the particle image displacement is large, since particle image displacements are small. Another uncertainty arises due to the fact that particle image pairs, i.e., the actual image of the particle and the image of the mirrored particle, lie very close to each other or even partly overlap on the sensor affecting the particle image location determination in a way that the wall-normal particle location becomes more uncertain. Also the interference of wall

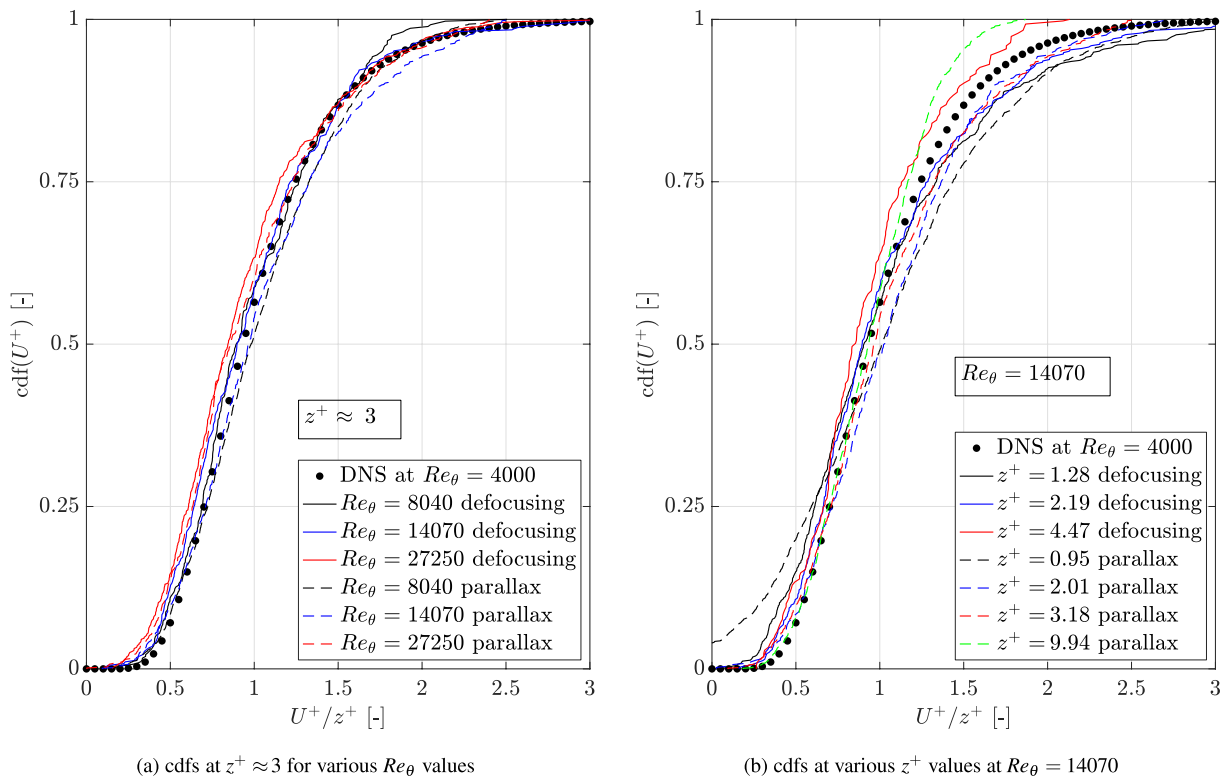


Fig. 10 cdfs of the measured data in comparison with a DNS reference set, performed at $Re_\theta = 4000$. In the viscous sublayer, at $z^+ < 5$, the cdf can be approximated by a log-normal distribution and it is supposed to have a self-similar character

reflections and the scattered light of the particles leads to the somewhat distorted intensity distributions of the particle images of particles that are very close to the wall, as in the $z^+ = 0.95$ case, around $20 \mu\text{m}$. Furthermore, the defocusing μPTV data at $z^+ = 4.49$ shows systematic deviations from the DNS reference, indicating the increasing uncertainties of the particle location determination with increasing wall-normal distance, as a result of the decreasing SNR of the particle images. However, the deviation of the green dashed line, representing parallax PTV data at $z^+ = 9.94$, outside of the viscous sublayer, shows the expected trend toward an asymmetric distribution above the viscous sublayer, as outlined by Alfredsson et al. (2011). Altogether, the comprehensive validation of the measurement results demonstrates that defocusing μPTV is a feasible concept for estimating the mean wall-shear-stress.

6 Conclusion

Defocusing μPTV is a feasible concept for the mean wall-shear-stress estimation, which is derived from the near-wall flow velocity data. A comparison with a parallax PTV reference measurement as well as several other diagnostic measures demonstrated the validity of this defocusing approach. This comprehensive validity investigation was of utmost importance, since there are a large number of processing parameters influencing the defocusing results; even the binning direction of the data is decisive, as well the vibration of the camera with respect to the measurement domain, among others.

In terms of limitations, the near-wall seeding supply is the biggest challenge of using particle imaging for near-wall flow measurements, in particular at larger U_e values. As such, a commercially available DEHS seeding generator with 45 Leskin nozzles was only able to provide enough seeding for the $U_e = 12.7\text{m/s}$ ($\text{Re}_\theta = 8040$) data set; for the other data sets, up to $U_e = 44.7\text{m/s}$ ($\text{Re}_\theta = 27250$), only a fog generator, operating with a water-glycol mixture, provided sufficient seeding close to the wall.

Altogether, this defocusing μPTV approach nicely complements larger scale measurements that require near-wall information such as scaling quantities. But also as a stand-alone technique, this defocusing approach is beneficial for determining the mean wall-shear-stress. For technical applications where $\bar{\tau}_w$ is an important measure, the ability to measure through a single, small optical access is crucial due to the often limited accessibility of such non-scientific facilities. In particular, since the proposed technique has the capability to measure through a curved surface, such that it is suitable to be employed for more complex shapes.

Author Contributions TF and MB wrote and reviewed the manuscript. CJK reviewed the manuscript.

Funding Open Access funding enabled and organized by Projekt DEAL. This work was not funded by third parties.

Data availability The raw data is available upon request.

Declarations

Conflict of interest The authors declare that there is no competing interest of financial or personal nature.

Ethical approval Not applicable.

Open Access This article is licensed under a Creative Commons Attribution 4.0 International License, which permits use, sharing, adaptation, distribution and reproduction in any medium or format, as long as you give appropriate credit to the original author(s) and the source, provide a link to the Creative Commons licence, and indicate if changes were made. The images or other third party material in this article are included in the article's Creative Commons licence, unless indicated otherwise in a credit line to the material. If material is not included in the article's Creative Commons licence and your intended use is not permitted by statutory regulation or exceeds the permitted use, you will need to obtain permission directly from the copyright holder. To view a copy of this licence, visit <http://creativecommons.org/licenses/by/4.0/>.

References

- Alfredsson PH, Örlü R, Schlatter P (2011) The viscous sublayer revisited-exploiting self-similarity to determine the wall position and friction velocity. *Exp Fluids* 51:271–280. <https://doi.org/10.1007/s00348-011-1048-8>
- Alfredsson PH, Örlü R (2010) The diagnostic plot - a litmus test for wall bounded turbulence data. *Eur J Mech- B/Fluids* 29:403–406. <https://doi.org/10.1016/j.euromechflu.2010.07.006>
- Amili O, Soria J (2011) A film-based wall shear stress sensor for wall-bounded turbulent flows. *Exp Fluids* 51:137–147. <https://doi.org/10.1007/s00348-010-1035-5>
- Amili O, Hind MD, Naughton JW, Soria J (2016) Evaluation of a film-based wall shear stress measurement technique in a turbulent channel flow. *Exp Ther Fluid Sci* 70:437–442. <https://doi.org/10.1016/j.expthermflusci.2015.09.027>
- Baars WJ, Squire DT, Talluru KM, Abbassi MR, Hutchins N, Marusic I (2016) Wall-drag measurements of smooth- and rough-wall turbulent boundary layers using a floating element. *Exp Fluids*. <https://doi.org/10.1007/s00348-016-2168-y>
- Baidya R, Baars WJ, Zimmerman S, Samie M, Hearst RJ, Dogan E, Mascotelli L, Zheng X, Bellani G, Talamelli A, Ganapathisubramani B, Hutchins N, Marusic I, Klewicki J, Monty JP (2019) Simultaneous skin friction and velocity measurements in high reynolds number pipe and boundary layer flows. *J Fluid Mech* 871:377–400. <https://doi.org/10.1017/jfm.2019.303>
- Barnkob R, Kähler CJ, Rossi M (2015) General defocusing particle tracking. *Lab on a Chip* 17:3556–3560. <https://doi.org/10.1039/c5lc00562k>
- Berghout P, Bullee PA, Fuchs T, Scharnowski S, Kähler CJ, Chung D, Lohse D, Huisman SG (2021) Characterizing the turbulent drag properties of rough surfaces with a taylor-couette set-up. *J Fluid Mech* 919:A45. <https://doi.org/10.1017/jfm.2021.413>

- Bross M, Fuchs T, Kähler CJ (2019) Interaction of coherent flow structures in adverse pressure gradient turbulent boundary layers. *J Fluid Mech* 873:287–321. <https://doi.org/10.1017/jfm.2019.408>
- Cierpka C, Rossi M, Segura R, Kähler CJ (2010) On the calibration of astigmatism particle tracking velocimetry for microflows. *Meas Sci Technol* 22(1):15401. <https://doi.org/10.1088/0957-0233/22/1/015401>
- Cierpka C, Segura R, Hain R, Kähler CJ (2010) A simple single camera 3C3D velocity measurement technique without errors due to depth of correlation and spatial averaging for microfluidics. *Meas Sci Technol* 21(4):045401. <https://doi.org/10.1088/0957-0233/21/4/045401>
- Cierpka C, Scharnowski S, Kähler C (2013) Parallax correction for precise near-wall flow investigations using particle imaging. *Appl Opt* 52(12):2923–2931. <https://doi.org/10.1364/AO.52.002923>
- Fernholz HH, Janke G, Schober M, Wagner PM, Warnack D (1996) New developments and applications of skin-friction measuring techniques. *Meas Sci Technol* 7:1396–1409
- Fuchs T, Hain R, Kähler CJ (2014) Three-dimensional location of micrometer-sized particles in macroscopic domains using astigmatic aberrations. *Opt Lett* 39(5):1298–1301. <https://doi.org/10.1364/OL.39.001298>
- Fuchs T, Hain R, Kähler CJ (2016) In situ calibrated defocusing PTV for wall-bounded measurement volumes. *Meas Sci Technol* 27(8):084005. <https://doi.org/10.1088/0957-0233/27/8/084005>
- Fuchs T, Hain R, Kähler CJ (2016) Uncertainty quantification of three-dimensional velocimetry techniques for small measurement depths. *Exp Fluids* 57(5):73. <https://doi.org/10.1007/s00348-016-2161-5>
- Fuchs T, Bross M, Scharnowski S, Kähler CJ (2018) Parallax corrected ptv for precise near wall boundary layer measurements
- Große S, Schröder W (2008) Mean wall-shear stress measurements using the micro-pillar shear-stress sensor MPS3. *Meas Sci Technol*. <https://doi.org/10.1088/0957-0233/19/1/015403>
- Huisman SG, Scharnowski S, Cierpka C, Kähler CJ, Lohse D, Sun C (2013) Logarithmic boundary layers in strong Taylor–Couette turbulence. *Phys Rev Lett* 110:264501. <https://doi.org/10.1103/PhysRevLett.110.264501>
- Jobe CE (1984) Prediction of aerodynamic drag. In: Air Force Wright Aero. Lab. Report No. AFWAL-TM-84-203, pp 1–99
- Kaplan EL, Meier P (1958) Nonparametric estimation from incomplete observations. *J Am Stat Assoc* 53:457–481. <https://doi.org/10.1080/01621459.1958.10501452>
- Knopp T, Schanz D, Novara M, Lühder W, Strampe L, Schülein E, Schröder A, Bross M, Parikh A, McLellan D, Eich F, Kähler CJ (2022) Experimental and numerical investigation of turbulent boundary layers with strong pressure gradients. In: AIAA SCITECH 2022 Forum. <https://doi.org/10.2514/6.2022-1035>
- Lee M, Moser RD (2015) Direct numerical simulation of turbulent channel flow up to. *J Fluid Mech* 774:395–415. <https://doi.org/10.1017/jfm.2015.268>
- Leister R, Fuchs T, Mattern P, Kriegseis J (2021) Flow-structure identification in a radially grooved open wet clutch by means of defocusing particle tracking velocimetry. *Exp Fluids* 62(2):29. <https://doi.org/10.1007/s00348-020-03116-0>
- Lunte J, Schülein E (2020) Wall shear stress measurements by white-light oil-film interferometry. *Exp Fluids*. <https://doi.org/10.1007/s00348-020-2917-9>
- Mckeon BJ, Smits AJ (2002) Static pressure correction in high reynolds number fully developed turbulent pipe flow. *Meas Sci Technol* 13:1608–1614
- Miozzi M, Capone A, Costantini M, Fratto L, Klein C, Felice FD (2019) Skin friction and coherent structures within a laminar separation bubble. *Exp Fluids*. <https://doi.org/10.1007/s00348-018-2651-8>
- Olsen MG, Adrian RJ (2000) Out-of-focus effects on particle image visibility and correlation in microscopic particle image velocimetry. *Exp Fluids* 29(1):S166–S174. <https://doi.org/10.1007/s003480070018>
- Örlü R, Vinuesa R (2020) Instantaneous wall-shear-stress measurements: advances and application to near-wall extreme events. *Meas Sci Technol*. <https://doi.org/10.1088/1361-6501/aba06f>
- Park JS, Kihm KD (2006) Three-dimensional micro-PTV using deconvolution microscopy. *Exp Fluids* 40(3):491–499. <https://doi.org/10.1007/s00348-005-0090-9>
- Perlin M, Dowling DR, Ceccio SL (2016) Freeman scholar review: passive and active skin-friction drag reduction in turbulent boundary layers. *J Fluids Eng Trans ASME*. <https://doi.org/10.1115/1.4033295>
- Samie M, Marusic I, Hutchins N, Fu MK, Fan Y, Hultmark M, Smits AJ (2018) Fully resolved measurements of turbulent boundary layer flows up to. *Journal of Fluid Mechanics* 851:391–415. <https://doi.org/10.1017/jfm.2018.508>
- Santiago JG, Wereley ST, Meinhart CD, Beebe DJ, Adrian RJ (1998) A particle image velocimetry system for microfluidics. *Exp Fluids* 25(4):316–319. <https://doi.org/10.1007/s003480050235>
- Schlatter P, Örlü R (2010) Assessment of direct numerical simulation data of turbulent boundary layers. *J Fluid Mech* 659:116–126. <https://doi.org/10.1017/S0022112010003113>
- Schlichting H, Gersten K (2016) *Boundary-Layer Theory*. Springer, Berlin Heidelberg. <https://doi.org/10.1007/978-3-662-52919-5>
- Schülein E (2014) Optical method for skin-friction measurements on fast-rotating blades. *Exp Fluids*. <https://doi.org/10.1007/s00348-014-1672-1>
- Smits AJ, Matheson N, Joubert PN (1983) Low-reynolds-number turbulent boundary layers in zero and favorable pressure gradients. *J Ship Res* 27:147–157. <https://doi.org/10.5957/jsr.1983.27.3.147>
- Smits AJ, Hultmark M, Lee M, Pirozzoli S, Wu X (2021) Reynolds stress scaling in the near-wall region of wall-bounded flows. *J Fluid Mech* 926:A31. <https://doi.org/10.1017/jfm.2021.736>
- Westerweel J, Geelhoed PF, Lindken R (2004) Single-pixel resolution ensemble correlation for micro-piv applications. *Exp Fluids* 37:375–384. <https://doi.org/10.1007/s00348-004-0826-y>
- Willert CE, Soria J, Stanislas M, Klinner J, Amili O, Eisfelder M, Cuvier C, Bellani G, Fiorini T, Talamelli A (2017) Near-wall statistics of a turbulent pipe flow at shear reynolds numbers up to 40 000. *J Fluid Mech* 826:R5. <https://doi.org/10.1017/jfm.2017.498>
- Wu M, Roberts JW, Buckley M (2005) Three-dimensional fluorescent particle tracking at micron-scale using a single camera. *Exp Fluids* 38(4):461–465. <https://doi.org/10.1007/s00348-004-0925-9>

Publisher's Note Springer Nature remains neutral with regard to jurisdictional claims in published maps and institutional affiliations.